

# Synthesis and Characterization of Microporous Fe–Si–O Materials with Tailored Iron Content from Silsesquioxane Precursors

Nicolae Maxim,<sup>†</sup> Arian Overweg,<sup>‡</sup> Patricia J. Kooyman,<sup>§</sup> Jos H. M. C. van Wolput,<sup>†</sup> Rob W. J. M. Hanssen,<sup>†</sup> Rutger A. van Santen,<sup>†</sup> and Hendrikus C. L. Abbenhuis\*,<sup>†</sup>

*Schuit Institute of Catalysis, Eindhoven University of Technology, P.O. Box 513, 5600 MB Eindhoven, The Netherlands, Interfacultair Reactor Instituut, Mekelweg 15, 2629 JB Delft, The Netherlands, and National Centre for HREM, Rotterdamseweg 137, 2628 AL Delft, The Netherlands*

*Received: September 13, 2001; In Final Form: November 10, 2001*

Calcination of mixtures of  $(\text{c-C}_5\text{H}_9)_7\text{Si}_7\text{O}_9(\text{OH})_3$ , **1**, and  $(\text{c-C}_5\text{H}_9)_7\text{Si}_7\text{O}_{12}\text{Fe}(\text{tmeda})$ , **2** ( $\text{tmeda} = N,N,N',N'$ -tetramethylethylenediamine), led to microporous amorphous Fe–Si–O materials with adjustable iron content in the range 1–11 wt %. A set of different complementary techniques including  $\text{N}_2$  physisorption, XRD, XPS, DRUV–vis, RS, IR, HRTEM, and Mössbauer spectroscopy was used to follow the variation of the textural properties, metal dispersion, and speciation with the iron content along the whole mixing series. The calcination of these mixtures produced Fe–Si–O materials having basically the same properties as those observed for the individually calcined iron silsesquioxane. The  $\text{N}_2$  physisorption indicates high surface areas, rather large pore volumes, and a very narrow pore size distribution with an average pore size diameter around 6–7 Å. The TEM and the spectroscopic analysis of the Fe–Si–O materials indicate that the iron is present mainly as small iron oxide particles highly dispersed throughout silica and to a minor extent as clustered and isolated species. The particle size distribution was estimated to be about 2–8 nm for 11% Fe–Si–O and 2–4 nm for samples with lower iron content. These materials showed catalytic activity in  $\text{NH}_3$  oxidation and  $\text{N}_2\text{O}$  decomposition.

## Introduction

Silsesquioxane chemistry attracts a substantial interest due to its applications in material science and catalysis. Metal-free silsesquioxanes are being used as precursors for ceramic materials.<sup>1</sup> Metallasilsesquioxanes can be used as well-defined homogeneous models for the active sites of supported catalysts or metal-containing zeolites.<sup>2</sup> They can even be active catalysts themselves, e.g. in epoxidation<sup>3</sup> or polymerization<sup>4</sup> of olefins. Metal-containing silsesquioxanes also turn out to be convenient precursors for potentially catalytic microporous amorphous M–Si–O materials with high surface area, uniformly controlled micropores, and high metal dispersion.<sup>5</sup> This development has also been stimulated by the fact that over the past decade a large number of metal silsesquioxane complexes have become available. Nowadays, the metals incorporated into the Si/O skeleton of silsesquioxanes include main group and early and late transition metals, as well as chalcogens.<sup>6</sup> The known literature already involves the calcination of Ti, Cr, Mg, Al, and Ga silsesquioxanes to form microporous mixed oxides.<sup>5</sup>

The sol–gel method can also be used to prepare mixed oxides or metal supported on silica. However, homogeneity of the multicomponent gels, in terms of the distribution of various components, strongly affects the properties of the final oxide.<sup>7</sup> For example, in the  $\text{TiO}_2$ – $\text{SiO}_2$  gel, titanium alkoxide hydrolyzes much faster than silicon alkoxide. Thus, hydrolysis of a liquid mixture of the two alkoxides would eventually result in the

formation of titanium oxide hydroxide clusters imbedded in the silica gel and segregation of  $\text{TiO}_2$  and  $\text{SiO}_2$  after calcination.<sup>8</sup>

The use of the metal silsesquioxane precursors guarantees that the metal and silicon are atomically mixed. Assuming that the water formed during calcination causes minor hydrolysis of the M–O–Si bonds and that the hydrolyzed metal species have low mobility, a uniform distribution of the metal throughout the silica is expected.

As described previously for chromium and aluminum silsesquioxanes, the calcination treatment resulted in the formation of metal oxide species highly dispersed throughout the amorphous silica.<sup>5b,c</sup> In both resulting M–Si–O materials the metal was mainly present in isolated sites. A minor amount of small metal oxide particles well dispersed throughout silica was observed as well. The resulting amorphous materials had a very narrow pore size distribution centered at 6 Å.

However, the metal content in the resulting M–Si–O materials (up to about 11 wt %) is fixed and depends on its concentration in the metal silsesquioxane precursors. To overcome this disadvantage for the potential catalytic applications of these materials, we propose here a way to adjust the metal content in the metallosilicate synthesis. Thus, we confirmed that calcination of metal-free silsesquioxanes gave rise to the formation of a microporous amorphous silica with a similar pore size distribution.<sup>5a,b</sup> In addition, metallasilsesquioxanes and silsesquioxanes are both soluble in solvents such as tetrahydrofuran.

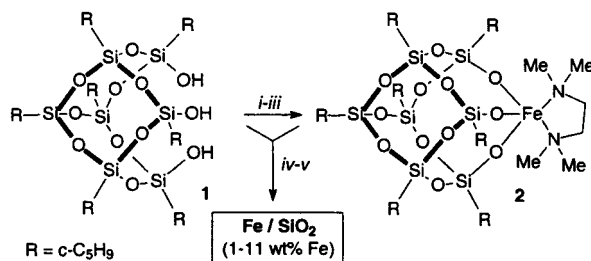
We now report the first application of a calcination procedure to the synthesis of a series of Fe–Si–O materials differing in iron content resulting from mixing a metal-free silsesquioxane

\* E-mail: H. C. L. Abbenhuis@tue.nl.

<sup>†</sup> Eindhoven University of Technology.

<sup>‡</sup> Interfacultair Reactor Instituut.

<sup>§</sup> National Centre for HREM.

**SCHEME 1: Silsesquioxane Route to Fe–Si–O Materials with Tailored Iron Content<sup>a</sup>**


<sup>a</sup> Reagents and conditions. (i) BuLi (3 equiv), THF, 20 °C, 5 min; (ii) FeCl<sub>3</sub> (1 equiv), 15 min; (iii) TMEDA (7.4 equiv), hexane, 18 h, 65% yield; (iv) mixture of **1** and **2**, THF; (v) calcination, O<sub>2</sub>/Ar, 500 °C, 4 h.

**1** and an iron silsesquioxane complex **2** in THF followed by removal of the solvent and calcination of the solid mixture.

We investigate here if the calcination of these mixtures leads to silica-based iron-containing materials having properties similar to those observed for the individually calcined iron silsesquioxane. Therefore, a set of different complementary techniques including N<sub>2</sub> physisorption, XRD, XPS, DRUV-vis, RS, IR, HRTEM, and Mössbauer spectroscopy was used to follow the variation of the textural properties, metal dispersion, and speciation with the iron content along the whole mixing series.

## Experimental Section

### Synthesis. Synthesis of Iron-Containing Silsesquioxane.

This was prepared according to a procedure based on a synthesis reported recently for the analogous compound (c-C<sub>6</sub>H<sub>11</sub>)<sub>7</sub>Si<sub>7</sub>O<sub>12</sub>-Fe(tmEDA).<sup>9</sup> The trisilanol silsesquioxane **1**<sup>10</sup> (6.23 g, 7.12 mmol) was dissolved in 125 mL of THF. Butyllithium (8.54 mL of a 2.5 M solution in hexane, 21.36 mmol) was added slowly to the solution of **1**. After mixing, a white precipitate was formed. When FeCl<sub>3</sub> (1.15 g, 7.12 mmol) was added, the white suspension changed its color from white to brown and after 15 min transformed into a brown transparent solution. After removal of the solvent in vacuo, addition of 125 mL of hexane, and hot filtration, a dark brown clear solution was obtained. Tmeda (8 mL, 53 mmol) was added to the filtrate and resulted in rapid formation of a light yellow solution. Keeping this solution at -30 °C for 1 day produced crystals of **2** in 65% yield. Elemental analyses were consistent with the calculated composition of complex **2**. Calcd: C, 47.15; H, 7.62; N, 2.68. Found: C, 47.13; H, 7.69; N, 2.61.

**Synthesis of Fe–Si–O Materials.** Fe–Si–O materials with iron contents from 11 wt % of iron (calcined complex **2**) down to 1 wt % were prepared by using different mixing ratios of compounds **1** and **2** (see Scheme 1). The solvent removal was performed from warm solutions under controlled vacuum and using vigorous stirring to ensure a good homogeneity of the resulting solid mixtures. Samples were calcined in batches of 0.5 g at 500 °C for 4 h in a flow of 20% O<sub>2</sub> in Ar. As reported earlier for calcination of chromium and magnesium silsesquioxane, these conditions allowed an efficient carbon removal and led to high surface area materials.<sup>5b,c</sup>

**Analysis.** The carbon content of M–Si–O materials was measured by heating the samples at 925 °C on a Perkin-Elmer Series II CHNS/O Analyzer 2400 automated analyzer.

Inductively coupled plasma optical emission spectrometry (ICP-OES) was used for the determination of the iron content in the Fe–Si–O materials. The measurements were performed

with a Spectro Cirosced spectrometer. Before measurement the samples were dried at 110 °C for 1 h and then dissolved in a mixture of HF and HNO<sub>3</sub> acids.

For nitrogen physisorption analysis, all samples were pre-treated in a vacuum at 200 °C for 2 h before the measurement. The measurements were performed on Micromeritics ASAP 2000 using an equilibration interval of 5 s and a low-pressure dose of 3.00 cm<sup>3</sup>/g at STP. Surface area, pore volume, and pore size distribution were calculated using the methods developed by Horvath–Kawazoe and Dubinin–Radushkevich.<sup>11</sup>

X-ray diffraction (XRD) data were collected on a Rigaku diffractometer in the range 5.0° < 2θ < 80° using Cu Kα radiation and the step scan method at 0.1 deg/min scanning speed and 5 s dwelling time.

X-ray photoelectron spectroscopy (XPS) measurements were obtained using a VG CLAM 2 spectrometer equipped with a Mg Kα source and a hemispherical analyzer. Measurements were carried out at 20 eV pass energy. Charging was corrected for by using the Si 2p peak of SiO<sub>2</sub> at 103.3 eV. The samples were ground and pressed in indium foil that was placed on a stainless steel stub. The XP spectra have been fitted with a VGS program fit routine, with a Shirley background subtraction and Gauss–Lorentz curves. The error in the binding energy was 0.2 eV. Elemental ratios were calculated from the peak areas with correction for the cross sections.<sup>12</sup>

Transmission electron microscopy (TEM) was performed using a Philips CM30UT high-resolution electron microscope with a field emission gun as a source of electrons operated at 300 kV. Samples were mounted on a microgrid carbon polymer supported on a copper grid by placing a few droplets of a suspension of ground sample in ethanol on the grid followed by drying at ambient conditions.

<sup>57</sup>Fe Mössbauer spectra were measured on a constant acceleration spectrometer in a triangular mode with a <sup>57</sup>Co:Rh source. Mössbauer spectra of all Fe–Si–O materials were recorded at 300 K. Additional measurements at 77 and 4.2 K were carried out for the Fe–Si–O samples containing 3, 7, and 11 wt % Fe, respectively. The overall spectra were deconvoluted with calculated Mössbauer spectra that consisted of Lorentzian-shape lines. In the case of quadrupole doublets the line widths and the absorption areas of the constituent lines were constrained equal. Positional parameters were not constrained in the fitting procedure. The isomer shift values are reported relative to sodium nitroprusside, Na<sub>2</sub>Fe(CN)<sub>5</sub>NO.

Diffuse reflectance UV–vis spectra (DRUV–vis) were taken at room temperature on a UV-2401PC Shimadzu spectrophotometer equipped with a diffuse reflectance unit. Grounded samples were loaded between 0.3 mm Suprasil windows. Spectra were recorded against a BaSO<sub>4</sub> reflectance standard in the range 190–1000 nm. The computer processing of the spectra consisted of the following steps: subtraction of the baseline; conversion to wavenumber; calculation of the Kubelka–Munk (KM) function.<sup>13</sup>

Fourier transform infrared (FTIR) spectra of the Fe–Si–O samples were performed under ambient conditions on a Nicolet Protégé 460 FTIR E.S.P. spectrometer equipped with a MCT/A detector and a Golden Gate single reflection diamond sampling unit. Automatic baseline correction of the spectra was used.

FTIR spectra of NO adsorbed on an 11% Fe–Si–O sample were measured on a Bruker FTIR spectrometer (IFS 113v) equipped with a vacuum cell. Self-supporting disks with a thickness of 8 mg·cm<sup>-2</sup> were used. The spectra were recorded by co-adding 500 scans at room temperature with a resolution of 4 cm<sup>-1</sup>. The samples were reduced in H<sub>2</sub> for 4 h at 673 K

**TABLE 1: Textural Properties and Composition of Fe–Si–O Materials**

sample	Fe (ICP) (wt %)	surf area <sup>a</sup> (m <sup>2</sup> ·g <sup>-1</sup> )	pore volume <sup>b</sup> (mL·g <sup>-1</sup> )		av pore diameter <sup>c</sup> (Å)	Fe/Si surf ratio (XPS)
11% Fe–Si–O	10.6	623	0.22	0.22	7.2	0.140
9% Fe–Si–O	8.3	662	0.24	0.23	7.1	0.110
7% Fe–Si–O	6.6	445	0.16	0.16	6.0	0.092
5% Fe–Si–O	4.9	561	0.20	0.19	6.3	0.063
3% Fe–Si–O	2.8	628	0.22	0.22	6.1	0.032
1% Fe–Si–O	0.9	548	0.19	0.19	5.9	0.011

<sup>a</sup> Estimated from the Dubinin–Radushkevich equation.<sup>11a</sup> <sup>b</sup> Estimated from the Dubinin–Radushkevich (left column)<sup>11a</sup> and Horvath–Kawazoe equations (right column).<sup>11b</sup> <sup>c</sup> Estimated from the Horvath–Kawazoe equation.<sup>11b</sup>

and evacuated in high vacuum ( $10^{-6}$  mbar) for 2 h. After the unloaded sample was cooled to room temperature, the spectrum was taken, followed by exposing the sample to NO gas for 30 min at a pressure of 130 mbar and recording of a new spectrum. After this, the loading of the samples was reduced stepwise by lowering the equilibrium pressure to 0.1 mbar as well as by desorption for 30 min at 298, 373, 498, and 653 K, respectively, followed by collecting room-temperature spectra after each step. The spectrum of the unloaded sample was subtracted from the spectra of samples with different NO loadings.

Raman spectra were recorded with a RFS 100/S FT-Raman Bruker spectrometer. A Nd:YAG laser at 1064 nm was used as the excitation source. Different laser powers in the range 40–180 mW were used. All spectra were recorded under ambient conditions by co-adding 1024 scans with a resolution of 4 cm<sup>-1</sup>.

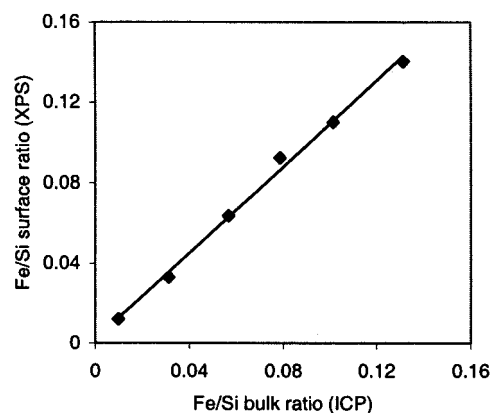
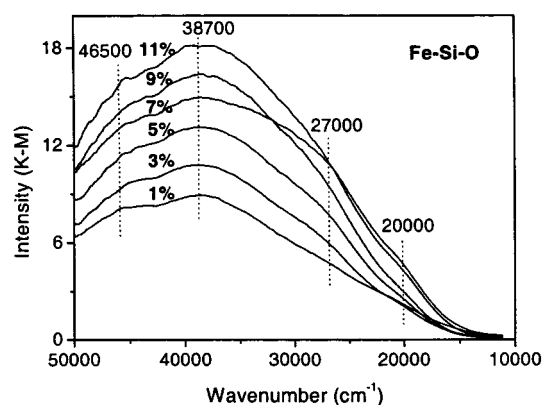
Fe–Si–O samples were tested in NH<sub>3</sub> oxidation and N<sub>2</sub>O decomposition. The catalytic tests were performed in continuous plug-flow reactors. Reaction conditions for NH<sub>3</sub> oxidation were the following: temperatures 200–400 °C; flow rate 50 N mL/min; NH<sub>3</sub> 1 vol %; O<sub>2</sub> 10 vol %; catalyst weight 0.1 g. Reaction conditions for N<sub>2</sub>O decomposition were the following: temperature 500 °C; flow rate 16 N mL/min; N<sub>2</sub>O 0.25 vol %; catalyst weight 0.04 g. The reaction products were analyzed by mass spectrometry and chemiluminescence methods.

## Results and Discussion

The nominal and actual iron bulk contents of the Fe–Si–O materials are shown in Table 1. The actual iron contents of the Fe–Si–O samples were analyzed by ICP-OES and are slightly in variance with the expected values. Unless otherwise notified, all iron loadings mentioned in the paper are referred to the nominal values. The carbon content of the samples determined by elemental analysis was about 0.2–0.4 wt %.

The textural properties of the Fe–Si–O materials were determined by using N<sub>2</sub> physisorption. All of the Fe–Si–O samples, excepting the 11% Fe–Si–O (calcined complex **2**), yielded type Ib isotherms characteristic of microporous materials. The 11% Fe–Si–O sample showed a type IIb isotherm associated with a steep increase in the adsorption amount at low  $p/p_0$ , indicative for the presence of both micro- and mesopores. Attribution of the Fe–Si–O materials isotherms was made according to extended IUPAC classification.<sup>14</sup>

Typical values for surface area, pore volume, and average pore diameter for Fe–Si–O materials are presented in Table 1. These results indicate the formation of microporous materials with large surface areas of about 500–600 m<sup>2</sup>/g, rather large pore volumes of ca. 0.2 mL/g, and a narrow pore size distribution with an average pore size diameter around 6–7 Å. Mesopore size distribution of the 11% Fe–Si–O estimated from the desorption isotherm by using the B–J–H method<sup>15</sup> indicated the formation of a few mesopores with a diameter of about 4 nm. For the Fe–Si–O samples with lower iron content no mesopores were detected.

**Figure 1.** Fe/Si atomic bulk ratio versus Fe/Si atomic surface ratio.**Figure 2.** Diffuse reflectance UV–vis spectra of the Fe–Si–O materials with different loadings.

The metal dispersion was estimated from XPS data. The surface Fe/Si atomic ratios obtained by XPS analysis are also presented in Table 1. The surface Fe/Si ratios were plotted against the bulk Fe/Si atomic ratios calculated from the actual iron concentrations, as shown in Figure 1. It can be seen that the Fe/Si surface and bulk ratios have a linear relationship along the whole Fe–Si–O series. The regression coefficient ( $R^2 = 0.9955$ ) and the slope of the line (1.0726) are very close to 1 indicating a good dispersion of iron throughout the silica for all the iron samples.

DRUV–vis spectroscopy is often used to identify the oxidation states and coordination environments of transition metal ions in supported metal oxide or zeolite catalysts.<sup>13</sup> The iron state in Fe–Si–O materials was investigated by DRUV–vis spectroscopy. DRUV–vis spectra of Fe–Si–O materials are shown in Figure 2. All of the Fe–Si–O samples show a strong and broad absorption extending from 50 000 to 12 000 cm<sup>-1</sup>. The intensity of the absorption spectra increases with the iron loading of the samples. Pure tetrahedral or octahedral Fe<sup>3+</sup> species are usually characterized by two distinct bands in the 50 000–40 000 cm<sup>-1</sup> region.<sup>16</sup> The presence, in this case, of



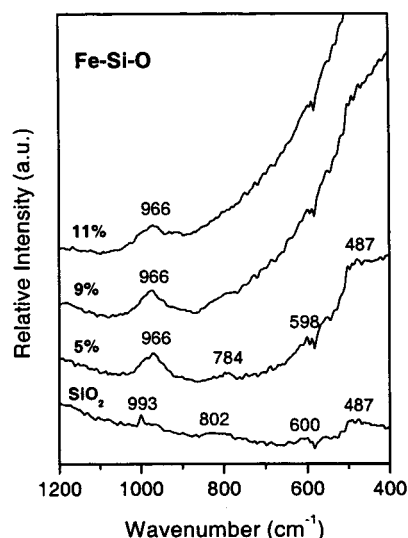


**Figure 3.** Raman spectra of the Fe-Si-O materials with different loadings.

an unresolved absorption suggests that the  $\text{Fe}^{3+}$  species can also have distorted symmetries. Two maxima can be distinguished in the DRUV-vis spectra of all of the Fe-Si-O materials at about 46 500 and 38 700  $\text{cm}^{-1}$ . The band at 46 500  $\text{cm}^{-1}$  was also found for Fe-silicalite, Fe-ZSM-5, and Fe-mesoporous silica and is ascribed to ligand-to-metal  $\text{Fe}^{3+}$  charge-transfer transitions involving isolated  $\text{Fe}^{3+}$  species with tetrahedral and/or octahedral coordination.<sup>17</sup> The band at 38 700  $\text{cm}^{-1}$  was also observed for Fe-silicalite after thermal treatments and assigned to clustered octahedral  $\text{Fe}^{3+}$  formed by migration of framework tetrahedral  $\text{Fe}^{3+}$  toward extraframework positions.<sup>17a</sup> Besides the isolated and clustered  $\text{Fe}^{3+}$ , additional iron species are also present as indicated by the two shoulders at about 27 000 and 20 000  $\text{cm}^{-1}$ . The latter band is characteristic of  $\text{Fe}_2\text{O}_3$  particles, while the former one is observed for example in  $\gamma$ - $\text{FeOOH}$  diluted in silica.<sup>18</sup> The data for the 7% Fe-Si-O sample markedly deviate from the others in the low-wavenumber region, where a stronger absorption and a broadening of the 27 000  $\text{cm}^{-1}$  band are observed. A newly prepared sample showed the same deviation, which we attributed to an increased contribution of ferric oxides particles for this sample. This could also result in blockage of some of the pores formed during calcination, explaining the somewhat lower surface area and pore volume of this sample. The origin of this deviation is not yet clearly understood, but the extent of this effect seems to be rather limited since the other techniques used did not reveal significant differences between the 7% Fe-Si-O and the other samples.

Thus, DRUV-vis spectra of Fe-Si-O materials indicate the presence in all the samples of both isolated and clustered  $\text{Fe}^{3+}$  species as well as of particles of iron oxide. A quantitative estimation of their concentration is however not reliable by reflectance spectroscopy.<sup>13</sup>

The Raman spectra of 11, 9, and 5% Fe-Si-O materials and of silica, obtained by calcination of metal-free silsesquioxane **1**, were measured under ambient conditions and are compared in Figure 3. The silica possesses weak Raman bands at  $\sim 487$ ,  $\sim 600$ ,  $\sim 802$ , and  $993 \text{ cm}^{-1}$ . The  $993 \text{ cm}^{-1}$  band is associated with Si-OH stretching mode of the surface hydroxyls. The broad bands at 600 and  $487 \text{ cm}^{-1}$  are assigned to D2 and D1 defect modes which have been attributed to tri- and tetracyclosiloxane rings produced via the condensation of surface hydroxyls.<sup>19</sup> The band at  $\sim 802 \text{ cm}^{-1}$  has been assigned to the

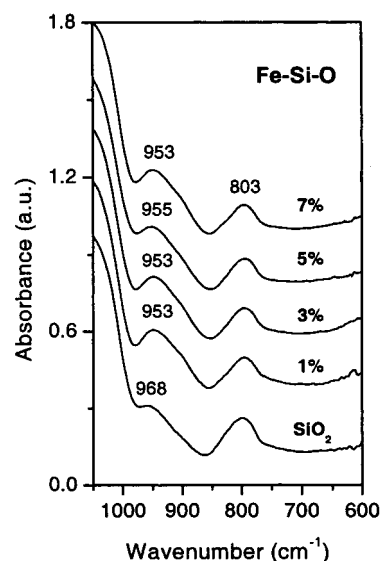


**Figure 4.** Infrared spectra of the Fe-Si-O samples.

symmetrical Si-O-Si stretching mode.<sup>20</sup> The changes in the silica Raman bands at  $\sim 600$  and  $\sim 487 \text{ cm}^{-1}$  are not very significant for the Fe-Si-O materials. However, accurate determination of the position of these bands is hindered by the strong fluorescence arising from the background of the samples. The  $\sim 802 \text{ cm}^{-1}$  band shifts downward to  $\sim 784 \text{ cm}^{-1}$  and becomes less broad, suggesting that some Si-O-Si bridges are affected by the dispersed iron oxide. A new silica band is observed at  $\sim 966 \text{ cm}^{-1}$  while the sharp band at  $993 \text{ cm}^{-1}$  is not visible anymore. A similar behavior observed for silica supported titania catalysts was attributed to the formation of Ti-O-Si bonds.<sup>21</sup> We also associated this  $27 \text{ cm}^{-1}$  shift with the presence of Fe-O-Si bonds. No bands characteristic for iron oxide or oxide hydroxide particles are observed, probably because some of these compounds are poor light scatterers. For example, the  $\gamma$ - $\text{Fe}_2\text{O}_3$  (maghemite), in contrast to  $\alpha$ - $\text{Fe}_2\text{O}_3$  (hematite) and  $\text{Fe}_3\text{O}_4$  (magnetite), has broad and poorly defined Raman bands of which resolution depends on the degree of crystallinity of the material. This makes the observation of such a phase very difficult.<sup>22</sup>

The IR spectra of 7, 5, 3, and 1% Fe-Si-O materials and of silica, obtained by calcination of metal-free silsesquioxane **1**, were measured under ambient conditions and are provided in Figure 4. Pure silica exhibits the symmetrical Si-O-Si stretching vibration at  $\sim 803 \text{ cm}^{-1}$ , along with a band at  $\sim 968 \text{ cm}^{-1}$  due to the symmetric stretch of Si-OH groups.<sup>23</sup> The  $\sim 968 \text{ cm}^{-1}$  band is observed for highly hydroxylated (high surface area) silicas, and its rather large half width is attributed to a hydrogen-bonding perturbation. The slight downward shift of this band from  $\sim 968$  to  $\sim 953 \text{ cm}^{-1}$ , observed for the Fe-Si-O samples, was assigned to the presence of some Fe-O-Si bonds in these materials.<sup>21a</sup>

Thus, Raman and IR spectra of Fe-Si-O materials both suggest the presence of some Fe-O-Si bonds. These techniques seem to be rather insensitive to the presence of iron oxide particles that is indicated by the DRUV-vis spectra.

However, additional information can be obtained by means of adsorption of a probe molecule. NO is particularly attractive from this point of view since its uptake on  $\text{Fe}_3\text{O}_4$  at 273 K and pressures near 10 kPa is 10 times higher than that of CO under similar conditions.<sup>24</sup> In addition, the extent of nitric oxide adsorption on silica is small at 273 K and subatmospheric pressures.<sup>25</sup> NO adsorption has been used to investigate iron

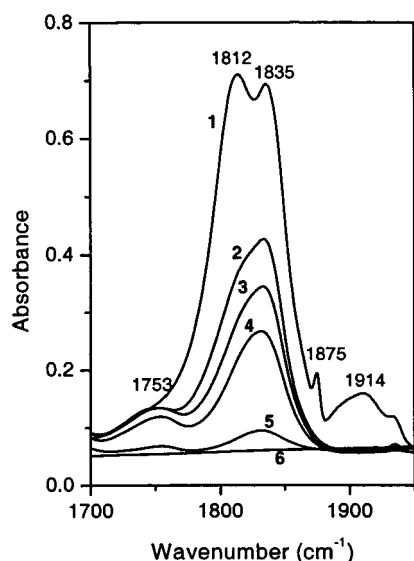


**Figure 5.** Room-temperature infrared spectra of 11% Fe–Si–O reduced in  $H_2$  at 673 K, exposed to NO, and evacuated at progressively higher temperatures: (1) at 298 K and 130 mbar; (2) at 298 K and 0.1 mbar; (3) after desorption at 298 K for 0.5 h; (4) after desorption at 373 K for 0.5 h; (5) after desorption at 498 K for 0.5 h; (6) after desorption at 653 K for 0.5 h.

speciation on silica-supported iron oxide and iron-containing zeolites.<sup>26</sup> Since NO adsorbs to very low extent on  $Fe^{3+}$  in comparison with  $Fe^{2+}$ , silica-supported iron oxide catalysts are reduced in hydrogen before NO adsorption.

The IR spectra of NO adsorbed on reduced 11% Fe–Si–O material (calcined 2) are shown in Figure 5. Only the wavenumber range from 1700 to 1950  $cm^{-1}$  is shown since all observable bands resulting from adsorbed NO were found within these limits. At maximum NO coverage, the spectrum is dominated by intense absorptions at 1812 and 1835  $cm^{-1}$ . Less intense features appear at 1914, 1875, and 1753  $cm^{-1}$ . Upon decrease of the NO pressure, the bands at 1914, 1875, and 1812  $cm^{-1}$  disappear. Only the 1835 and 1753  $cm^{-1}$  bands survive at the room-temperature evacuation step. This doublet is not destroyed even after outgassing the sample under high vacuum at 498 K. It is worth noticing that the initial spectrum (curve 1) is recovered by readmission of NO. Similar bands have been reported for NO adsorption on silica-supported iron oxide and Fe–silicalite.<sup>26</sup> These bands were attributed to nitrosyl complexes formed by NO adsorption on ferrous species present in two different coordinative states. In the Fe/SiO<sub>2</sub> case, the doublet appearing at 1914 and 1812  $cm^{-1}$  and the single band at 1753  $cm^{-1}$  were respectively assigned to di- and mononitrosyl species formed on 4-fold-coordinated  $Fe^{2+}$  centers strongly interacting with the support, while the band at 1835  $cm^{-1}$  was assigned to a mononitrosyl complex on 6-fold-coordinated  $Fe^{2+}$  at the surface of small iron oxide particles. The disappearance of the 1914 and 1812  $cm^{-1}$  bands upon evacuation was attributed to the conversion of dinitrosyl to mononitrosyl complexes that are more stable at low pressures.<sup>26a</sup> In the Fe–silicalite case, the number of NO ligands involved in the formation of nitrosyl complexes and the equilibria between these complexes were rather differently interpreted. However, similar ferrous species were taken into consideration, namely, low-coordinated iron species present as isolated iron centers grafted to the framework and high-coordinated iron species belonging to  $(FeO)_n$  extra-framework (or partially extraframework) clusters.<sup>26c</sup> According to these assignments, the IR spectra of NO adsorbed on 11% Fe–Si–O indicate the presence of both isolated iron species

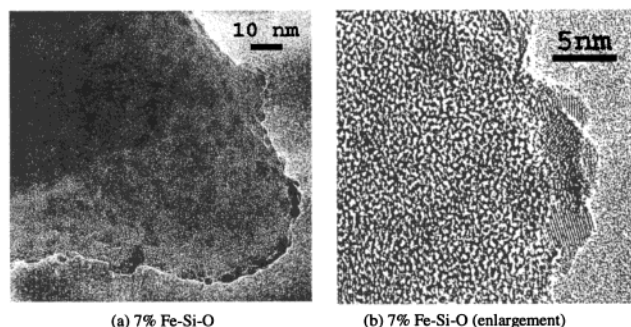


**Figure 6.** TEM micrographs of (a) 7% Fe–Si–O and (b) 7% Fe–Si–O (zoom in).

and clusters or small particles of iron oxide. These findings are in agreement with the interpretation of DRUV–vis, Raman, and IR spectra.

Transmission electron microscopy is routinely used to investigate the dispersion and size of the metal oxide particles on the support surface. However, observing the metal dispersion with TEM requires sufficient contrast between the metal oxide and the support, and it can be difficult to detect small and highly dispersed metal oxide particles. Nevertheless, Fe–Si–O materials were examined with high-resolution TEM, which allowed us to obtain good images of thin areas of the samples as exemplified in Figure 6 for the 7% Fe–Si–O sample. In this micrograph well-dispersed particles (Figure 6a) presenting lattice fringes (Figure 6b) can be seen on the silica surface. Similar pictures were obtained for the other Fe–Si–O samples (not shown here for sake of brevity). The particle size distribution seems to narrow with the decrease of the iron content. Thus, the particle size on the 11% Fe–Si–O sample was in the 2–8 nm range while on the 3, 5, and 7% Fe–Si–O samples mainly particles of 2–4 nm size were observed. The small size of these crystalline particles explains why they were not detected by XRD. It should also be noted that some of the particles seem to be amorphous (no lattice fringe patterns are present). Since the XRD patterns of the Fe–Si–O materials present only a broad band around 20–30° in  $2\theta$  angle usually assigned to amorphous silica,<sup>27</sup> identification of the nature of these particles is rather difficult. However, the measurements of lattice fringe spacings of the small crystalline phases ( $d = 2.10$ , 2.52, and 2.95 Å) and comparison with reference XRD data for iron oxides and several iron silicates indicated that they are most probably  $\gamma$ -Fe<sub>2</sub>O<sub>3</sub>, maghemite ( $d = 2.09$ , 2.52, and 2.95 Å; JCPDS file No. 15-0615). The presence of such an iron oxide phase explains also why it could not be observed in the Raman spectra of Fe–Si–O materials.

TEM results are in good agreement with the DRUV–vis and IR spectra of adsorbed NO. They clearly indicate the formation of iron oxide particles. This implies that, during the calcination procedure, the Fe–O–Si bonds can be hydrolyzed by the water formed from combustion of the organic part of the silsesquioxanes. This allows the migration of the metal species on the nascent silica surface with the final formation of metal oxide particles. The tendency to form smaller iron oxide particles with the lowering of the iron content might be attributed to the fact that, in the precursor mixtures containing less iron, the hydrolyzed iron species has to travel longer distances on the silica to form particles of iron oxide. This minimizes the chance to form large particles and favors the formation of smaller ones.

The chemical state of iron in Fe–Si–O materials was also investigated by means of Mössbauer spectroscopy. <sup>57</sup>Fe Mössbauer spectra of all Fe–Si–O materials were measured at 300

K. In all cases a single quadrupole doublet was obtained with isomer shifts (IS) of  $0.61 \pm 0.01$  mm/s and quadrupole splittings (QS) ranging from 1.01 to 1.11 mm/s. These parameters are all very similar and indicate  $\text{Fe}^{3+}$  ions in a high-spin state for all Fe–Si–O materials.

Additional information on the particle size distribution of small iron oxide particles in these materials was obtained by studying the temperature dependence of the Mössbauer spectra. This information is based on the magnetic properties of the small iron oxide particles, which depend on both the temperature and the particle volume of these iron oxide particles.<sup>28</sup>

Temperature-dependent Mössbauer spectra of 3, 7, and 11% Fe–Si–O samples are given in Figure 7a–c. The corresponding Mössbauer parameters are given in Table 2. In all three figures, a temperature-related transition in the spectra can be observed from a quadrupole doublet to a sextuplet. This transition is related to a slowing down of the rate of fluctuation of the magnetization vector among the easy directions of the small iron oxide particles such that the particles become magnetic on the time scale of the Mössbauer experiment. In that case a magnetically split Mössbauer spectrum, i.e. a sextuplet, is obtained. For the 3 and 7% Fe–Si–O samples, this transition takes place on lowering the temperature of the Mössbauer measurement from 77 to 4.2 K. A more gradual transition is observed for the 11% Fe–Si–O material. There, next to the quadrupole doublet, a sextuplet is already visible at 77 K that becomes more prominent at 4.2 K. In addition, the Mössbauer spectrum of the latter material still shows a quadrupole doublet at 4.2 K. Such a doublet is not observed in the 4.2 K Mössbauer spectra of the 3 and 7% Fe–Si–O materials. Thus, the 11% Fe–Si–O sample has an estimated particle size distribution ranging from smaller than 2 nm to about 6 nm. The samples containing less iron on the other hand have a much narrower particle size distribution, with an approximated particle size of ca. 2 nm. The absence of a quadrupole doublet at 4.2 K in the Mössbauer spectra of these two samples indicates that no iron oxide clusters of sizes smaller than 2 nm (too small to give a sextuplet at 4.2 K) are detected. This could be related on one hand to the lower concentrations of iron, which makes it more difficult to distinguish the quadrupole doublet from the sextuplet at 4.2 K, and on the other hand to a low amount of isolated species and very small clusters of iron oxide compared with the iron oxide particles.

Mössbauer spectra indicate that small iron oxide particles are the main iron species in the Fe–Si–O materials. The particle size distributions estimated from these spectra are very close to those observed with HRTEM and confirm the narrowing of the particle size range with the decrease of the iron content.

The predominance of iron oxide particles in the Fe–Si–O materials suggests a different behavior of the iron silsesquioxane during calcination in comparison with the aluminum or chromium silsesquioxane where mainly isolated metal oxide species were detected after calcination.<sup>5b,c</sup> This could be related to the different propensity to hydrolysis of M–O–Si bonds from different metallasilsesquioxanes. It is known that the large predisposition of iron precursors to hydrolysis restricts its incorporation in zeolite frameworks to very low concentrations.<sup>29</sup> The high dispersion of iron in Fe–Si–O materials should therefore be associated with a low mobility of the hydrolyzed iron species which hamper the formation of bulk iron oxide and help to preserve the high dispersion from the initial precursors mixture.

Iron-based catalysts have been widely used in reactions such as ammonia and Fischer–Tropsch synthesis and more recently

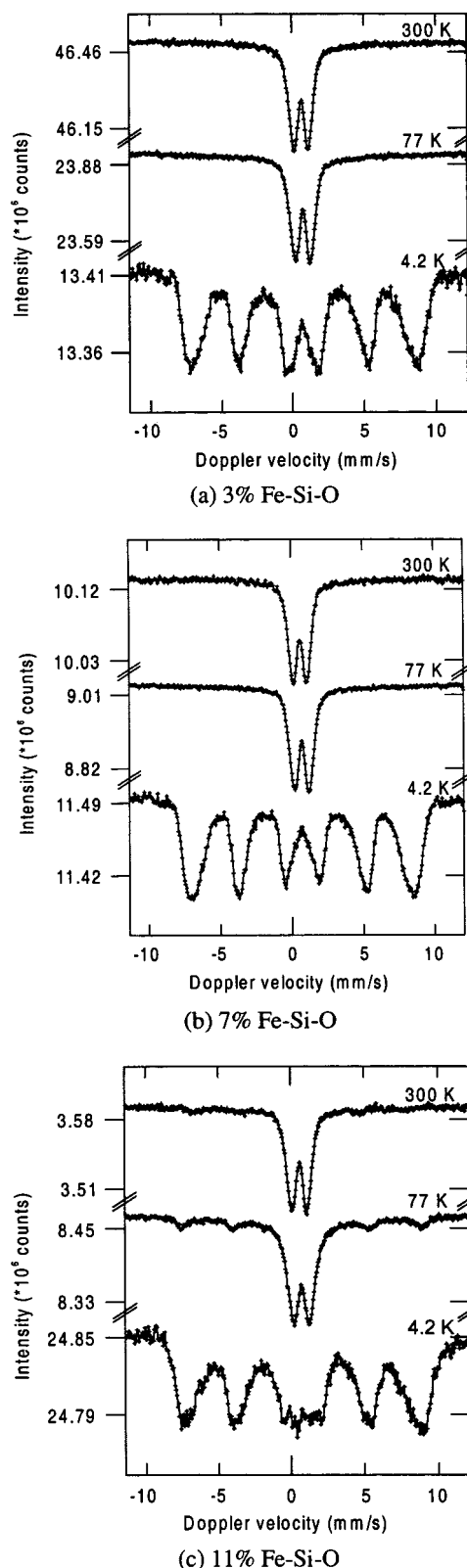


**Figure 7.** Mössbauer spectra of (a) 3% Fe–Si–O, (b) 7% Fe–Si–O, and (c) 11% Fe–Si–O recorded at 300, 77, and 4.2 K.

for the hydroxylation of benzene and methane. Here the Fe–Si–O catalysts have been tested in ammonia oxidation and  $\text{N}_2\text{O}$  decomposition.

The Fe–Si–O catalysts have been tested in  $\text{NH}_3$  oxidation at 400 °C. The 11% Fe–Si–O sample catalyzed the selective oxidation of  $\text{NH}_3$  to  $\text{N}_2$  and  $\text{H}_2\text{O}$  with 76% conversion and 95% selectivity. This catalyst, when pretreated in  $\text{H}_2$  before reaction,



**TABLE 2: Parameters Belonging to Mössbauer Spectra of Fe–Si–O Materials with Different Loadings**

sample	measurement condition (T, K)	isomer shift (mm/s)	quadrupole splitting (mm/s)	hyperfine field (T)	spectral contribution (%)
3% Fe–Si–O	300	0.61	1.05		100
	77	0.71	1.12		100
	4.2	0.72		47.2	82
		0.68		6.3	18
7% Fe–Si–O	300	0.61	1.01		100
	77	0.71	1.07		100
	4.2	0.72		47.2	88
		0.74		7.0	12
11% Fe–Si–O	300	0.62	1.06		100
	77	0.73	1.12		72
		0.72		50.6	28
	4.2	0.76		47.8	83
		0.72	1.08		17

gave 84% conversion and 97% selectivity. The reduced 5% Fe–Si–O sample gave 58% conversion and 96% selectivity.

The reduced 11% and 5% Fe–Si–O catalysts were tested in N<sub>2</sub>O decomposition to N<sub>2</sub> and O<sub>2</sub> at 500 °C and gave 20% and 5% conversion, respectively. Extensive testing of the catalytic properties of this series of iron catalysts is in progress, and it will be reported later.

## Conclusions

We proposed a successful way to prepare microporous amorphous Fe–Si–O materials with adjustable iron content in the range 1–11 wt % via calcination of mixtures of metal-free silsesquioxane **1** and iron silsesquioxane complex **2**.

Examination of the textural properties, metal dispersion, and speciation along the whole mixing series showed that calcination of the silsesquioxane precursor mixtures led to Fe–Si–O materials having properties similar to those observed for the individually calcined iron silsesquioxane.

The N<sub>2</sub> physisorption indicates high surface areas, rather large pore volumes, and a very narrow pore size distribution with an average pore size diameter around 6–7 Å. TEM and spectroscopic analysis showed that the iron is present mainly as small iron oxide particles highly dispersed throughout silica and to a minor extent as clustered and isolated species. Most of the iron oxide particles are crystalline, but some amorphous particles seem to be present too. An increased formation of ferric oxides particles is indicated by DRUV–vis spectra in the case of 7% Fe–Si–O sample, but the extent of this effect seems to be rather limited since the other techniques used did not reveal significant differences between this sample and the others.

Fe–Si–O materials catalyzed the selective oxidation of NH<sub>3</sub> to N<sub>2</sub> and H<sub>2</sub>O. They also showed activity in N<sub>2</sub>O decomposition.

In conclusion, we demonstrated the efficiency of this approach to overcome the disadvantage of the fixed metal content associated with calcination of individual metallasilsesquioxanes. This increases the applicability of the metallasilsesquioxane precursors for the synthesis of new microporous metallosilicate catalysts, and it opens a way to prepare microporous mixed oxide catalysts containing more than one metal.

**Acknowledgment.** This work was supported in part (N.M., P.J.K.) by the Council for Chemical Sciences of The Netherlands Organization for Scientific Research (NWO-CW). Dr. Ir. L. Coulier is gratefully acknowledged for his support with the XPS. Ms. A.M. Elemans-Mehring is acknowledged for OES-ICP measurements.

## References and Notes

- (1) (a) Baney, R. H.; Itoh, M.; Sakakibara, A.; Suzuki, T. *Chem. Rev.* **1995**, 95, 1409. (b) Agaskar, P. A. *Chem. Commun.* **1992**, 1024. (c) Mantz, R. A.; Jones, P. F.; Chaffee, K. P.; Lichtenhan, J. D.; Gilman, J. W. *Chem. Mater.* **1996**, 8, 1250.
- (2) Feher, F. J.; Budzichowski, T. A. *Polyhedron* **1995**, 14, 3239.
- (3) (a) Maschmeyer, T.; Klunduk, M. C.; Martin, C. M.; Shephard, D. S.; Thomas, J. M.; Johnson, B. F. G. *Chem. Commun.* **1997**, 1847. (b) Crocker, M.; Herold, R. H. M.; Orpen, A. G. *Chem. Commun.* **1997**, 2411.
- (4) (a) Duchateau, R.; Abbenhuis, H. C. L.; van Santen, R. A.; Meetsma, A.; Thiele, S. K. H.; van Tol, M. F. H. *Organometallics* **1998**, 17, 5663. (b) Duchateau, R.; Cremer, U.; Harmsen, R. J.; Mohamud, S. I.; Abbenhuis, H. C. L.; van Santen, R. A.; Meetsma, A.; Thiele, S. K. H.; van Tol, M. F. H.; Kranenburg, M. *Organometallics* **1999**, 18, 5447.
- (5) (a) Wada, K.; Nakashita, M.; Bundo, M.; Ito, K.; Kondo, T.; Mitsudo, T. *Chem. Lett.* **1998**, 659. (b) Maxim, N.; Abbenhuis, H. C. L.; Stobbelaar, P. J.; Mojjet, B. L.; van Santen, R. A. *Phys. Chem. Chem. Phys.* **1999**, 18, 4473. (c) Maxim, N.; Magusin, P. C. M. M.; Kooyman, P. J.; van Wolput, J. H. M. C.; van Santen, R. A.; Abbenhuis, H. C. L. *Chem. Mater.* **2001**, 13, 2958. (d) Wada, K.; Yamada, K.; Kondo, T.; Mitsudo, T. *Chem. Lett.* **2001**, 12.
- (6) Voronkov, M. G.; Lavrent'yev, V. I. *Top. Curr. Chem.* **1982**, 102, 199. (b) Lorenz, V.; Fischer, A.; Giebmann, S.; Gilje, J. W.; Gun'ko, Y.; Jacob, K.; Edelmann, F. T. *Coord. Chem. Rev.* **2000**, 206–207, 321. (c) Abbenhuis, H. C. L. *Chem.–Eur. J.* **2000**, 6, 25.
- (7) Kung, H. H.; Ko, E. I. *Chem. Eng. J.* **1996**, 64, 203.
- (8) Hutter, H.; Mallat, T.; Baiker, A. *J. Catal.* **1995**, 153, 177.
- (9) Lorenz, V.; Fischer, A.; Edelmann, F. T. *Z. Anorg. Allg. Chem.* **2000**, 626, 1728.
- (10) Feher, F. J.; Budzichowski, T. A.; Blanski, R. L.; Weller, K. J.; Ziller, J. W. *Organometallics* **1991**, 10, 2526.
- (11) (a) Dubinin, M. M.; Radushkevich, L. V. *Proc. Acad. Sci. U.S.S.R.* **1947**, 55, 331. (b) Horwath, G.; Kawazoe, K. *J. Chem. Eng. Japan* **1983**, 16, 470.
- (12) Scofield, J. H. *J. Electron Spectrosc. Relat. Phenom.* **1976**, 8, 129.
- (13) Weckhuysen, B. M.; Schoonheydt, R. A. *Catal. Today* **1999**, 49, 441.
- (14) Rouquerol, F.; Rouquerol, J.; Sing, K. *Adsorption by Powders & Porous Solids-Principles, Methodology and Applications*; Academic Press: London, 1999.
- (15) Barrett, E. P.; Joyner, L. G.; Halenda, P. P. *J. Am. Chem. Soc.* **1951**, 73, 373.
- (16) (a) Bordiga, S.; Geobaldo, F.; Lamberti, C.; Zecchina, A.; Boscherini, F.; Genoni, F.; Leofanti, G.; Petrini, G.; Padovan, M.; Geremia, S.; Vlaic, G. *Nucl. Instrum. Methods B* **1995**, 97, 23. (b) Figgis, B. N. *Introduction to Ligand Fields*; Wiley: New York, 1966.
- (17) (a) Bordiga, S.; Buzzoni, R.; Geobaldo, F.; Lamberti, C.; Giamello, E.; Zecchina, A.; Leofanti, G.; Petrini, G.; Tozzola, G.; Vlaic, G. *J. Catal.* **1996**, 158, 486. (b) Centi, G.; Vazzana, F. *Catal. Today* **1999**, 53, 683. (c) Tuel, A.; Arcon, I.; Millet, J. M. M. *J. Chem. Soc., Faraday Trans.* **1998**, 94, 3501.
- (18) Bongiovanni, R.; Pellizzetti, E.; Borgarello, E.; Meisel, D. *Chim. Ind.* **1994**, 93, 261.
- (19) (a) Morrow, B. A.; Mcfarlan, A. J. *J. Non-Cryst. Solids* **1990**, 120, 61. (b) Brinker, C. J.; Kirkpatrick, R. J.; Tallant, D. R.; Bunker, B. C.; Montez, B. *J. Non-Cryst. Solids* **1988**, 99, 418.
- (20) MacMillan, P. *Am. Mineral.* **1986**, 69, 622.
- (21) (a) Gao, X.; Bare, S. R.; Fierro, J. L. G.; Banares, M. A.; Wachs, I. E. *J. Phys. Chem. B* **1998**, 102, 5653. (b) Pei, S.; Zajac, G. W.; Kaduk, J. A.; Faber, J.; Boyanov, B. I.; Duck, D.; Fazzini, D.; Morrison, I. T.; Yang, D. S. *Catal. Lett.* **1993**, 21, 333.
- (22) (a) de Faria, D. L. A.; Silva, S. V.; de Oliveira, M. T. *J. Raman Spectrosc.* **1997**, 28, 873. (b) Perez-Robles, F.; Garcia-Rodriguez, F. J.; Jimenez-Sandoval, S.; Gonzales-Hernandez, J. *J. Raman Spectrosc.* **1999**, 30, 1099.
- (23) (a) Boccuti, M. R.; Rao, K. M.; Zecchina, A.; Leofanti, G.; Petrini, G. *Stud. Surf. Sci. Catal.* **1989**, 48, 133. (b) Vansant, E. F.; Voort, P. V. D.; Vrancken, K. C. *Stud. Surf. Sci. Catal.* **1995**, 93. (c) Zecchina, A.; Bordiga, S.; Spoto, S.; Marchese, L.; Petrini, G.; Leofanti, G.; Padovan, M. *J. Phys. Chem.* **1992**, 96, 4985.
- (24) Kubsh, J. E.; Chen, Y.; Dumesic, J. A. *J. Catal.* **1981**, 71, 192.
- (25) Solbakken, A.; Reyerson, L. H. *J. Phys. Chem.* **1959**, 63, 1622.
- (26) (a) Yuen, S.; Chen, Y.; Kubsh, J. E.; Dumesic, J. A.; Topsoe, N.; Topsoe, H. *J. Phys. Chem.* **1982**, 86, 3022. (b) Bocuzzi, F.; Guglielminotti, E.; Pinna, F.; Signoreto, M. *J. Chem. Soc., Faraday Trans.* **1995**, 91 (18), 3237. (c) Spoto, G.; Zecchina, A.; Berlier, G.; Bordiga, S.; Clerici, M. G.; Basini, L. *J. Mol. Catal. A* **2000**, 158, 107.
- (27) Real, C.; Alcalá, M. D.; Criado, J. M. *J. Am. Ceram. Soc.* **1996**, 79, 2012.
- (28) Mørup, S. *Hyperfine Interact.* **1990**, 60, 959.
- (29) Fejes, P.; Nagy, J. B.; Lazar, K.; Halasz, J. *Appl. Catal., A* **2000**, 190, 117.